JOURNAL OF APPLIED CRYSTALLOGRAPHY

ISSN 1600-5767

Structural refinement of $BaMgF_4$ from X-ray diffraction ferroelectric switching contrasts

N. Leubner,[a,b,c] C. Richter,[c] I. Biran,[a] G. Bonetti,[c] H. Tanaka,[c] S. Polo-Filsan,[c] B. J. Campbell[d] and S. Gorfman[a,e]*

[a]Department of Materials Science and Engineering, Tel Aviv University, Israel, [b]Institute of Experimental Physics, TU Bergakademie Freiberg, Germany, [c]Leibniz-Institut für Kristallzüchtung, Berlin, Germany, [d]Department of Physics and Astronomy, Brigham Young University, Utah, USA, and [e]Smart Ferroic Materials Center, University of Arkansas, USA. *Correspondence e-mail: gorfman@tauex.tau.ac.il

Received 26 June 2026
Accepted 4 October 2026

Edited by R. Guinebretière, Institut de Recherche sur les Céramiques, France

Keywords: *in situ* X-ray diffraction; resonant scattering; ferroelectricity; symmetry-mode analysis; single-crystal structure refinement.

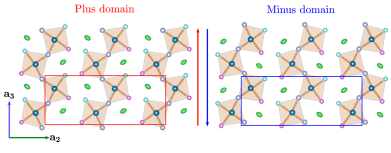
Supporting information: this article has supporting information at journals.iucr.org/j

Understanding the distortions of the crystal structure that accompany a paraelectric–ferroelectric phase transition is essential for elucidating the origin of ferroelectricity. Such distortions can, however, be difficult to characterize by X-ray diffraction because they are small and often obscured by the presence of multiple ferroelectric domains, X-ray absorption and extinction. These limitations complicate conventional structure refinement, especially when implemented during *in situ* polarization reversal under an electric field. Here, we present a structure-refinement strategy based on electric-field-induced Bragg intensity contrasts measured during reversible polarization switching. These data emphasize symmetry-breaking distortions while being insensitive to absorption and scale-factor effects. The method is formulated using group-theoretic symmetry-mode parameters referenced to a parent paraelectric structure. The approach is applied to the polarization switching in uniaxial ferroelectric $BaMgF_4$ using *in situ* single-crystal X-ray diffraction with resonant scattering at the Cu $K\alpha_1$ wavelength. Refinement against 42 experimentally determined intensity contrasts yields displacive mode amplitudes consistent with previously reported structural models. The agreement improves significantly when refinement of anisotropic atomic displacement parameters is included. Complementary analysis of electric-field-induced Bragg peak shifts provides the field dependence of the strain tensor components and corresponding piezoelectric coefficients. The contrast-based refinement strategy demonstrated here is applicable to other uniaxial ferroelectrics and offers a robust X-ray crystallographic route for isolating symmetry-breaking structural distortions in *in situ* diffraction experiments.

1. Introduction

Switchable ferroelectricity arises when a symmetry-lowering phase transition transforms the non-polar paraelectric parent phase into the polar ferroelectric child phase (Lines & Glass, 1979; Aizu, 1966). Both the ferroelectric state and the transition itself are of great fundamental and practical interest because many functional properties, including dielectricity, piezoelectricity and pyroelectricity, are strongly enhanced by ferroelectricity (Park & Shrout, 1997; Damjanovic, 1998; Haertling, 1999; Kreisel *et al.*, 2009; Trolier-McKinstry *et al.*, 2018; Uchino, 2017).

Characterizing these structural distortions, both statically and during polarization switching, is essential for understanding the origin of ferroelectricity and related physical properties. Yet, several complicating factors make this task one of the central challenges in X-ray crystallography. First, the atomic displacements responsible for spontaneous polarization are often within the sub-picometre range. Second,



OPEN ACCESS
Published under a CC BY 4.0 licence

ferroelectric crystals typically exist in multi-domain states, causing Bragg reflections to split into components that overlap partially or completely. This means that additional refinement parameters are required to account for the volumetric ratio of domains in the beam, such as the Flack parameter for the case of inversion domains (Flack, 1983; Flack & Bernardinelli, 1999; Flack & Shmueli, 2007). Third, conventional X-ray structure analysis requires application of oblique incidence, polarization, Lorentz (Warren, 1990) and absorption corrections to the measured diffraction intensities. While the first three corrections are well established, absorption remains problematic, particularly in *in situ* polarization switching experiments due to the presence of electrodes, wires and silver paste traces. Finally, the extinction correction further reduces the accuracy of the refined structural model (Becker & Coppens, 1974).

Taken together, these factors undermine the reliability of traditional X-ray crystallographic techniques for the characterization of polarization switching. This encourages the development of alternative methods capable of isolating the structural parameters responsible for ferroelectricity. This goal is of broad significance in both crystallography and materials science.

Several attempts have been made to perform crystallographic refinement using single-crystal X-ray diffraction data in a way that avoids the uncertainties associated with absorption and overall scale factor as well as diminishing the possible effect of extinction. For example, Parsons *et al.* (2013) proposed a refinement strategy based on the ratios of the measured intensities of Friedel/Bijvoet pairs $I(\mathbf{h})/I(\bar{\mathbf{h}})$. As noted there, on traditional four-circle X-ray diffractometers with point detectors, the pair ($\mathbf{h}$, $\bar{\mathbf{h}}$) could be measured by changing the diffractometer angles from $(2\theta, \omega, \chi, \varphi)$ to $(-2\theta, -\omega, \chi, \varphi)$, thus ensuring identical beam paths through the sample and therefore identical absorption and extinction corrections. However, most modern X-ray diffractometers employ area detectors, where Friedel/Bijvoet reflections are accessed using inequivalent reflection geometries with the assumption of identical correction factors being no longer valid.

A similar strategy was pursued by Gorfman and co-workers (Gorfman *et al.*, 2006; Schmidt *et al.*, 2009; Gorfman *et al.*, 2013), who exploited relative changes of diffraction intensities to extract electric-field-induced atomic displacements. These studies, however, were limited to non-ferroelectric piezoelectric crystals. Furthermore, Gorfman *et al.* (2016) demonstrated how the combination of resonant scattering and ferroelectric switching can be used to obtain structural information in a $BaTiO_3$-based ferroelectric. Their work was based, however, on *in situ* powder X-ray diffraction and, given the simplicity of the structural model, used the intensity and position of a single Bragg peak. A comparable approach relying on Bragg intensity ratios, rather than absolute intensities, was implemented by Ozawa *et al.* (1998) to investigate light-induced structural changes.

Here we extend the relative-intensity concept to a full single-crystal structure-refinement strategy. The method is based on measuring Bragg intensities under an external electric field that reversibly switches the spontaneous polarization of the crystal. For each reflection $\mathbf{h}$, the pair of measured intensities $I^{\uparrow}(\mathbf{h})$ and $I^{\downarrow}(\mathbf{h})$ corresponding to the opposite polarization states are then used to define the relative intensity contrast:

$$C_{\rm obs}(\mathbf{h}) = 2\frac{I^{\uparrow}(\mathbf{h}) - I^{\downarrow}(\mathbf{h})}{I^{\uparrow}(\mathbf{h}) + I^{\downarrow}(\mathbf{h})}. \quad (1)$$

The key advantage of this approach is that $I^{\uparrow}(\mathbf{h})$ and $I^{\downarrow}(\mathbf{h})$ are measured at exactly the same diffractometer angles and position of the peak on the detector, making the refinement completely independent of absorption and scale-factor corrections. In addition, unlike absolute intensities, the corresponding intensity contrasts emphasize structural changes directly associated with ferroelectric switching. Finally, because these contrasts are sensitive to deviations from the high-symmetry paraelectric phase, this method is particularly well suited for symmetry-mode analysis using the *ISODISTORT* program (Campbell *et al.*, 2006) of the *ISOTROPY* software suite (https://iso.byu.edu).

We apply this methodology to $BaMgF_4$ (BMF), a uniaxial ferroelectric fluoride with a relatively simple crystal structure and reliable switchability. Beyond serving as a model system for methodological development, BMF is also an attractive material in its own right, particularly for ultraviolet laser-optics applications, further underscoring the importance of accurate structural characterization (Herr *et al.*, 2023).

2. The structure of $BaMgF_4$

2.1. Ferroelectric and paraelectric phases

BMF belongs to the family of ternary fluorides $BaMF_4$ (where M = Mn, Zn, Mg, Cu *etc.*), which have been extensively studied for their structural and ferroic properties (Ederer & Spaldin, 2006; Garcia-Castro *et al.*, 2018). At room temperature, BMF crystallizes in the orthorhombic space group type $Cmc2_1$ (No. 36) (Gingl, 1997; Posse *et al.*, 2009) with conventional lattice parameters a = 4.13, b = 14.51, c = 5.82 Å and $Z = 4$ formula units per conventional unit cell. There are a total of $N_{\rm p} = 12$ ($N_{\rm c} = 24$) atoms in the primitive (conventional) unit cell. The structure consists of corner-sharing MgF_6 octahedra arranged in layers, separated by Ba atoms. The structure retains $Cmc2_1$ symmetry down to 10 K (Posse *et al.*, 2011), showing only a slight regularization of the MgF_6 octahedra upon cooling. Nuclear magnetic resonance, electron paramagnetic resonance and Raman spectroscopy revealed subtle local rearrangements of the octahedra near 240 K, although the average symmetry remains unchanged (Kowalczyk *et al.*, 2011). In this work, we refer to the two reported structures as S1 (Gingl, 1997) and S2 (Posse *et al.*, 2009).

The higher-symmetry paraelectric phase is estimated to occur above the melting point (DiDomenico *et al.*, 1969). However, high-pressure studies have shown that BMF undergoes a reversible $Cmc2_1$ (No. 36) $\rightarrow$ $Cmcm$ (No. 63)

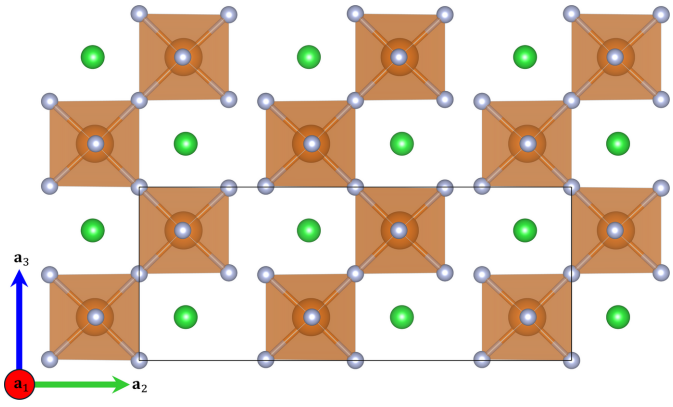


Figure 1
Schematic drawing of the optimized parent (S0) *Cmcm* structure of $BaMgF_4$ viewed along the $\mathbf{a}_1$ axis of the conventional unit cell. The figure highlights the layered arrangement of corner-sharing MgF_6 octahedra (brown) stacked perpendicular to $\mathbf{a}_2$, with Ba atoms (green spheres) accommodated in the interlayer cavities. This centrosymmetric parent structure serves as the reference for distortions leading to the polar $Cmc2_1$ phase as an isotropy subgroup of *Cmcm*. Figure created using *VESTA* (Momma & Izumi, 2011).

transition near 6 GPa (Posse *et al.*, 2011). Accordingly, we constructed the hypothetical *Cmcm* (No. 63) parent phase using the *FINDSYM*/*ISOCIF* programs (Stokes & Hatch, 2005; https://iso.byu.edu/). Further details of this phase are provided below and in Fig. 1.

2.2. Symmetry-mode analysis of $BaMF_4$

As is common in symmetry-mode (SM) analysis, we introduce the collective displacements of Ba, Mg and F atoms, which transform the structure of the paraelectric parent into the ferroelectric child. The atomic displacements involved in this *Cmcm* (No. 63) → $Cmc2_1$ (No. 36) phase transition are described by $N_M = 12$ symmetry modes (indexed by m) with $N_D = 2$ symmetry-related domains, indexed by δ (assuming the ferroelectric nature of domains we also use the illustrative indices ↑ and ↓ instead of 1 and 2). The SM analysis describes the position vector $\mathbf{r}_\mu^\delta$ of the μth atom of the conventional unit cell and domain δ relative to the corresponding position vector $\mathbf{r}_\mu^0$ of the same atom in the undistorted child:

$$\mathbf{r}_\mu^\delta = \mathbf{r}_\mu^0 + \sum_{m=1}^{N_M} \mathbf{D}_{\mu m} A_m^\delta. \tag{2}$$

$\mathbf{D}_{\mu m}$ is the three-dimensional mode-definition vector for atom μ and mode m; A_m^δ is the scalar amplitude of mode m in domain δ. The term $\mathbf{D}_{\mu m} A_m^\delta$ describes the contribution of the mth SM to the atomic displacement $\Delta\mathbf{r}_\mu^\delta$ in domain δ. Importantly, the definition of $\mathbf{D}_{\mu m}$ absorbs any mode-normalization factor so the amplitude of each SM has Å units and is numerically equal to the root-summed-squared displacement induced by the mode throughout the primitive child cell:

$$\left|A_m^\delta\right| = \left(\sum_{\mu=1}^{N_P} \left|\mathbf{D}_{\mu m} A_m^\delta\right|^2\right)^{1/2}. \tag{3}$$

We sometimes omit the superscript from the mode amplitude components $A_m^\delta \equiv A_m$ of the reference domain ↑. The transformation to the other domain is given by

$$A_n^\delta = \sum_{m=1}^{N_M} T_{nm}^\delta A_m. \tag{4}$$

The square matrix with components T_{nm}^δ has a block-diagonal form with each block being the representation matrix of the coset representative of domain δ for an irreducible representation (IR) of the parent space group that contributes to the child structure. All SM information, such as mode labels (Bradley & Cracknell, 2009), relevant IR matrices and SM definitions $\mathbf{D}_{\mu m}$, is extracted from the output of *ISODISTORT*. The geometrical meaning of each SM can be conveniently visualized using the related *ISOVIZ* tool.

For the *Cmcm* (No. 63) → $Cmc2_1$ (No. 36) transition in BMF, $N_M = 12$ modes belong to the one-dimensional IRs Γ_1^+ and Γ_2^- of the parent *Cmcm* space group type. The five Γ_1^+ modes preserve the symmetry of the parent, while the seven Γ_2^- modes give rise to the $Cmc2_1$ space group type of the child. The one-dimensional character of these IRs means that the components $T_{nm}^\downarrow$ form a diagonal matrix with $T_{nn}^\downarrow = \bar{1}$ for Γ_2^- and $T_{nn}^\downarrow = +1$ for Γ_1^+ modes. If we collect the seven order parameters of Γ_2^- into 'a' and the five order parameters of Γ_1^+ into 'b' then the order parameter of the child structure has two ferroelectric domains:

$$\uparrow (\mathrm{a}|\mathrm{b}) \quad \text{and} \quad \downarrow (\bar{\mathrm{a}}|\mathrm{b}). \tag{5}$$

Two aspects deserve attention in the following discussion. First, in the absence of any experimentally reported parent structure of BMF, we constructed one ourselves. The first step was to apply the FINDSYM feature within *ISOCIF* to detect and enforce the approximate symmetries of the child to obtain a *Cmcm* parent structure. This proved to have five displacive structural parameters, which *ISODISTORT* parametrized as Γ_1^+ SM amplitudes. We then varied these five amplitudes in order to minimize the distortions of MgF_6 octahedra and BaF_{13} coordination polyhedra. Their aggregate distortion was quantified using the parameter $F = D + L + B$, which combines the contributions from the six Mg—F bond lengths d_α, the 12 F—F edge lengths l_β and the 13 Ba—F bond lengths b_γ:

$$D = \sum_{\alpha=1}^{6} \frac{(d_\alpha - \bar{d})^2}{6\bar{d}^2}, \quad L = \sum_{\beta=1}^{12} \frac{(l_\beta - \bar{l})^2}{12\bar{l}^2}, \quad B = \sum_{\gamma=1}^{13} \frac{(b_\gamma - \bar{b})^2}{13\bar{b}^2}. \tag{6}$$

Here $\bar{d}$, $\bar{l}$ and $\bar{b}$ are the arithmetic means of the six Mg—F bond lengths, the 12 F—F edge lengths and the 13 Ba—F bond lengths, respectively. The minimization of F was performed using a custom MATLAB script. The obtained Γ_1^+ SM amplitudes were then reintroduced into *ISODISTORT* to generate the reference optimized parent structure (Fig. 1), hereafter referred to as S0.

Second, the description of any polar structure is influenced by the floating unit cell origin problem. For the $Cmc2_1$ space group type, the origin can be chosen anywhere along the 2_1

axis parallel to [001]. As a result, structures reported by different investigators may be shifted relative to one another along this axis, complicating direct comparisons. To avoid this problem, we choose the child structure that is as close as possible to S0. To achieve this, we fold the [001] sliding motion of the entire structure into a vector of fixed displacive SM amplitudes B_m, which may have non-zero contributions from the ferroelectric Γ_2^- IRs only (see Appendix *A* for more details). The sliding is accomplished by replacing the affected SM amplitudes A_m with $A_m + tB_m$ and minimizing

$$f = \sum_{m=1}^{N_M} (A_m + tB_m)^2 \tag{7}$$

with respect to parameter t. This allows us to calculate the shift magnitude as

$$t = -\frac{\sum_{m=1}^{N_M} A_m B_m}{\sum_{m=1}^{N_M} B_m^2}. \tag{8}$$

Equation (8) can be used to eliminate the ambiguity in choosing the unit cell origin. This is an important step which allows us to compare structures reported by different investigators using the corresponding mode's amplitude. The next section demonstrates the application of this method for the two structures of BMF reported in the literature.

2.3. Summarizing the existing structural data

Tables 1–4 summarize the structural data (reference domain ↑) obtained as illustrated in Fig. 2. Table 1 presents the bond-valence sum (BVS) for MgF_6 octahedra in the S0, S1 and S2 structures. BVS is defined according to (Brown, 2006; Brown & Altermatt, 1985)

$$\mathrm{BVS} = \sum_{\alpha=1}^{6} \exp\left(\frac{1.578 - d_\alpha}{0.37}\right). \tag{9}$$

It is expected to be close to 2 (the valence of the Mg atom).

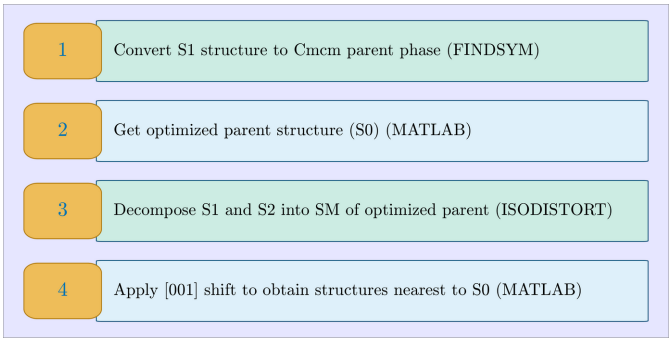


Figure 2
Workflow of the algorithm for the comparison between the existing structures. This first step results in finding an arbitrary realization of the parent *Cmcm* phase. The second step applies the available degrees of freedom to find the realization of the same phase with the lowest possible distortion of MgF_6 octahedra and BaF_{13} polyhedra. The next step obtains the SM amplitudes describing the S1/S2 structures relative to the optimized parent S0 from the previous step. The last step corrects the obtained SM amplitudes $A_m \rightarrow A_m + tB_m$ according to equation (8).

Table 1
The structure-validation parameters for the S0, S1 and S2 structures.

The first line shows the corresponding BVS of the Mg atom as defined in equation (9), the next two lines show corresponding MgF_6 octahedral distortion parameters D and L, and the last line presents the BaF_{13} bond-length variance as defined in equation (6).

	S0	S1	S2
BVS Mg	1.56	1.93	1.96
D (10^{-3})	0.01	0.71	0.82
L (10^{-3})	0.20	1.28	1.30
B (10^{-3})	0.23	7.55	7.59

Table 2
The optimized parent (S0) structure: atom labels, Wyckoff positions (WP, including multiplicities) and fractional coordinates.

Note that, given the artificial character of this structure, the quantities are presented without uncertainties.

Atom label	WP	x	y	z
Ba1	4*c*	0	0.608	1/4
Mg1	4*c*	0	0.898	1/4
F1	4*a*	0	0	0
F2	8*f*	0	0.207	−0.006
F3	4*c*	0	0.399	1/4

Table 3
Comparison of the $Cmc2_1$ S1 and S2 structures using SM analysis.

The first two columns provide the SM number and names (the numbering and naming of modes according to *ISODISTORT*). The third column indicates if the corresponding SM is 'ferroelectric' (F) or not (N). The fourth and fifth columns show the SM amplitudes corresponding to the S1 and S2 structures. Importantly, the uncertainty about the unit cell origin was eliminated using the algorithm described above and equation (8).

MN	Mode label (*Cmcm*[0,0,0]...)	Ferroelectric	$A^{(S1)}$ (Å)	$A^{(S2)}$ (Å)
1	GM2-(a)[Ba1:c:dsp]B1(a)	F	0.243	0.235
3	GM2-(a)[Mg1:c:dsp]B1(a)	F	−0.047	−0.046
6	GM2-(a)[F1:a:dsp]Bu_2(a)	F	−0.550	−0.547
8	GM2-(a)[F2:f:dsp]A′_2(a)	F	0.331	0.339
11	GM2-(a)[F3:c:dsp]B1(a)	F	−0.115	−0.122
5	GM2-(a)[F1:a:dsp]Bu_1(a)	N	−0.500	−0.503
7	GM2-(a)[F2:f:dsp]A′_1(a)	N	−0.429	−0.438
2	GM1+(a)[Ba1:c:dsp]A1(a)	N	0.837	0.837
4	GM1+(a)[Mg1:c:dsp]A1(a)	N	0.355	0.348
9	GM1+(a)[F2:f:dsp]A′_1(a)	N	−0.747	−0.776
10	GM1+(a)[F2:f:dsp]A′_2(a)	N	−0.147	−0.165
12	GM1+(a)[F3:c:dsp]A1(a)	N	0.453	0.446

Table 1 presents polyhedral distortion parameters [equation (6)]. Minimizing the distortions of MgF_6 and BaF_{13} polyhedra yields a rather low bond-valence sum for Mg (BVS = 1.56 instead of the expected 2.0). This deviation is consistent with the tendency of the structure to undergo distortion into the ferroelectric phase.

Table 2 lists the crystallographic coordinates x_μ, y_μ, z_μ of the five symmetry-independent atoms in the optimized *Cmcm* parent phase, expressed relative to the conventional unit-cell-based vectors $\mathbf{a}_1, \mathbf{a}_2, \mathbf{a}_3$:

$$\mathbf{r}_\mu = x_\mu \mathbf{a}_1 + y_\mu \mathbf{a}_2 + z_\mu \mathbf{a}_3. \tag{10}$$

Tables 3 and 4 compare the S1 and S2 structures. These data were obtained by mode decomposition of the S1 and S2

Table 4
Comparison of the $Cmc2_1$ S1 and S2 structures using coordinates of atoms in the unit cell.

These coordinates were obtained by applying the mode amplitudes in Table 3 to the optimized *Cmcm* parent phase in Table 2.

Atom label	WP	x (S1, S2)	y (S1)	y (S2)	z (S1)	z (S2)
Ba1	4*a*	0	0.6483	0.6483	0.2795	0.2786
Mg1	4*a*	0	0.9148	0.9145	0.2444	0.2444
F1	4*a*	0	−0.0244	−0.0245	−0.0668	−0.0664
$F2_1$	4*a*	0	0.1666	0.1653	0.0103	0.0094
$F2_2$	4*a*	0	0.8038	0.8045	0.0467	0.0489
F3	4*a*	0	0.4214	0.4211	0.2361	0.2352

structures relative to S0 using *ISODISTORT* method 4, followed by the modification of the corresponding SM amplitudes according to equations (7) and (8). Table 3 includes the SM labels and their amplitudes. Γ_2^- SMs resulting in non-zero average shift along [001] are explicitly marked as 'ferroelectric' (F), while the remaining modes are labeled as 'non-ferroelectric' (N). Table 4 presents the same comparison in terms of the atomic coordinates within the conventional unit cell.

3. Experiment

3.1. *In situ* X-ray diffraction during polarization switching

A BMF single crystal was grown at the Leibniz Institute for Crystal Growth (Berlin, Germany) and prepared as an $h = 0.3$ mm thick plate. Thin gold electrodes were deposited on the major plate surfaces, enabling the application of an external electric field along [001].

Single-crystal X-ray diffraction measurements were carried out on a home-laboratory four-circle X-ray diffractometer at Tel Aviv University (Gorfman *et al.*, 2021). The instrument is equipped with a micro-focused Cu X-ray source, a Ge(220) channel-cut monochromator (fully suppressing the Cu $K\alpha_2$ line), a four-circle Huber goniometer and a PILATUS 1M pixel area detector. Besides the standard crystallographic tasks (determination of lattice parameters/crystal orientation), the diffractometer enables high-resolution three-dimensional reciprocal-space mapping under an external electric field, as implemented previously (*e.g.* Gorfman *et al.*, 2020; Choe *et al.*, 2018; Vasiljevic *et al.*, 2022). A schematic of the experimental arrangement is shown in Fig. 3.

The crystal was mounted on a custom-designed sample holder that provided electrical contact while preserving wide reciprocal-space accessibility in reflection geometry. A Moku: Pro (https://download.liquidinstruments.com/documentation/specs/hardware/mokupro/MokuPro-Specifications.pdf) multi-instrument system was used as a real-time data logger (V and I inputs in Fig. 3) and waveform generator producing a bipolar triangular waveform with a frequency of $f = 0.01$ Hz (period $T = 100$ s), which was amplified by a Matsusada high-voltage amplifier (gain 200). This resulted in a maximum voltage $V_{max} = 600$ V, corresponding to a peak electric field of $E_{max} = V_{max}/h = 20$ kV cm^{-1}, sufficient to induce a complete polarization reversal. The voltage across the sample and the current flowing through it were continuously monitored using a 100:1 voltage divider and 1 kΩ resistor, respectively. Note that the relatively low electric-field cycling frequency of 0.01 Hz was selected primarily to operate the detector at 1 frame s^{-1}, allowing each electric-field cycle to be sampled by 100 detector frames. The measured switching current

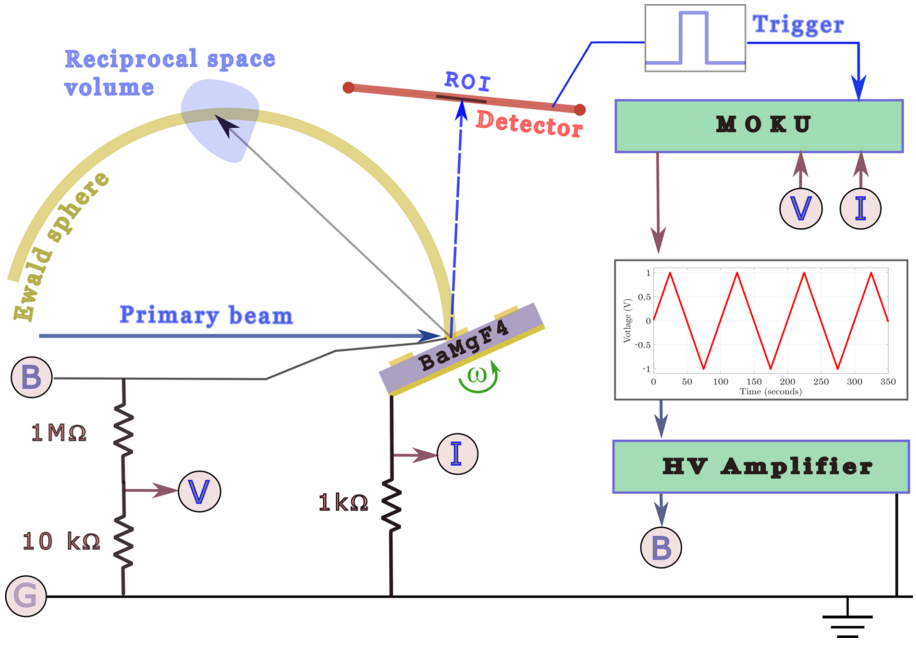


Figure 3
A schematic drawing of the X-ray diffraction experiment and synchronization with the external electric field applied to the crystal. Here 'MOKU' is a multi-instrument system, combining digital oscilloscope, data logger and function generator. 'Detector' is a PILATUS 1M pixel area detector. 'HV Amplifier' is a MATSUSADA amplifier, providing a voltage gain factor of 200.

confirmed that polarization reversal was completed well within each half-cycle.

Following the determination of the crystal orientation using *CrysAlisPro* (Meyer, 2015), we recorded a series of electric-field-dependent 3D reciprocal-space maps around $N_{obs} = 42$ different Bragg reflections. Each map was acquired in ω step-scan mode (ω is the standard angle of the four-circle diffractometer), covering approximately 0.3° centered on the Bragg reflection and sampling $N_\omega = 101$ points (100 intervals). The ω motor was automatically advanced to the next position every $T = 100$ s, *i.e.* after the completion of a full voltage period, while each detector frame was exposed for 1 s. In this manner, the electric-field cycle was uniformly sampled by $N_E = 100$ detector frames at every ω position, so that the full scan was composed of $N_\omega N_E$ detector frames. Accordingly, the acquisition time of one reflection was 2 h 48 min. All detector frames were subsequently reordered to reconstruct the electric-field dependence of the reciprocal-space intensity distribution using custom on-site MATLAB scripts.

To maximize the information content of the experimentally accessible dataset, the measured reflections were selected to provide broad reciprocal-space coverage in terms of reflection indices and the orientation of the reciprocal-lattice vector relative to the applied electric field. In addition, using the S1 structural model, we evaluated the sensitivity of the calculated intensity contrasts to variations of each of the 12 SM amplitudes. Reflections were selected from those exhibiting the highest sensitivity to the different amplitudes, thereby ensuring sensitivity to a broad range of structural degrees of freedom. Finally, reflections with calculated squared structure factors below 5% of that of the reference 004 reflection were excluded to ensure sufficient diffracted intensity.

3.2. Examples of measured data

Fig. 4 presents a partial summary of the experiment corresponding to the $\bar{1}76$ reflection. Similar figures for other reflections are provided in Supplementary Information 1. Fig. 4(*a*) shows a false-color map of the rocking curve as a function of time and ω angle. It includes $N_E = 100$ consecutive rocking curves, each corresponding to a specific time and applied electric field. Fig. 4(*b*) displays the time dependence of the applied electric field and the average current (extracted from the voltage/current monitor readings). Here electric field is marked as positive/negative if it points along [001]/$[00\bar{1}]$, respectively.

Figs. 4(*c*) and 4(*d*) show the electric-field dependence of the integrated intensity (in relative units) and the position of the center of mass of the ω rocking curve. Note that, in addition to the displacement of the ω rocking curve, similar displacements were observed in all the reciprocal-space directions: the analysis in the following section implements the shifts in radial directions. Most importantly, the integrated intensity exhibits very clear ferroelectric hysteresis behavior and switching between almost stationary $I^{\uparrow}(\mathbf{h})$ and $I^{\downarrow}(\mathbf{h})$ values. The corresponding switching contrast $C_{obs}(\mathbf{h})$ is defined as in equation (1).

The electric current in Fig. 4(*b*) is averaged over 101 electric-field cycles applied during the entire measurement of the reflection. To underline the difference between the average and momentary behavior, Fig. 5 displays the electric-field dependence of the current over three individual voltage cycles, showing the typical sharp Barkhausen-like pulses. These pulses correspond to individual switching events (Tagantsev *et al.*, 2010) and appear statistically distributed in their position

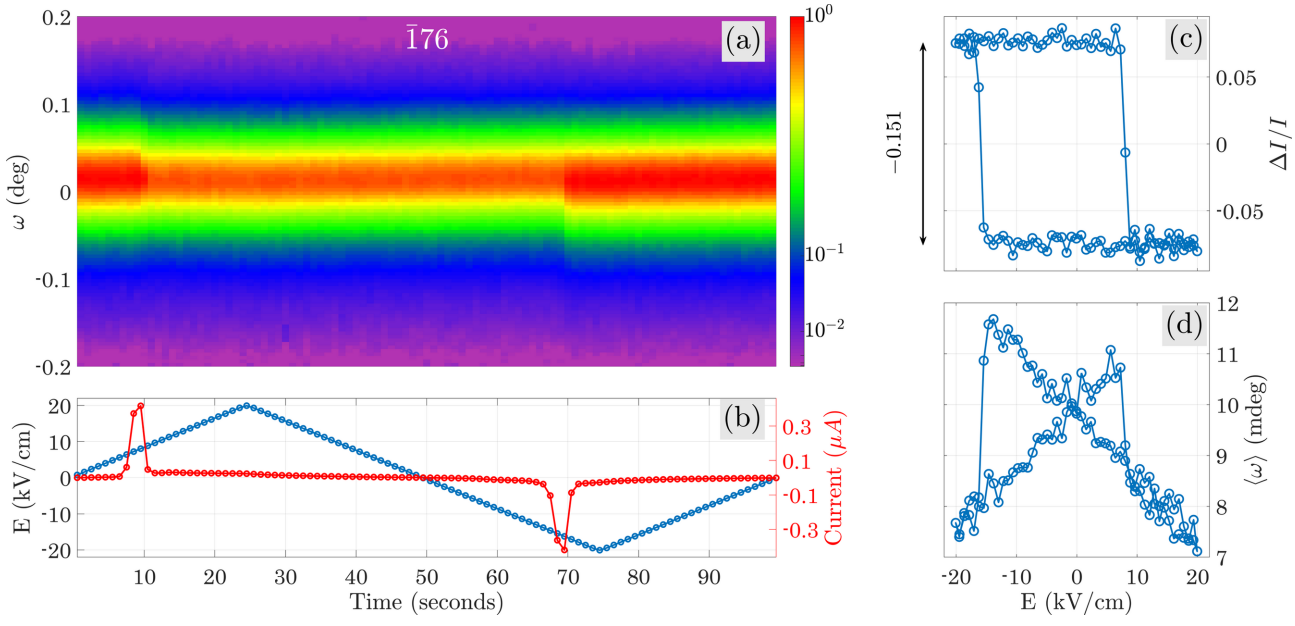


Figure 4
The average evolution of the $\bar{1}76$ Bragg reflection rocking curve during the electric-field cycle. (*a*) False-color time–ω map showing $N_E = 100$ consecutive rocking curves on a logarithmic intensity scale. (*b*) Applied electric field (blue) and the average of the measured current (red) versus time. (*c*) Normalized intensity changes $\Delta I/\langle I\rangle$ and (*d*) center-of-mass position of the ω rocking curve as functions of the electric field.

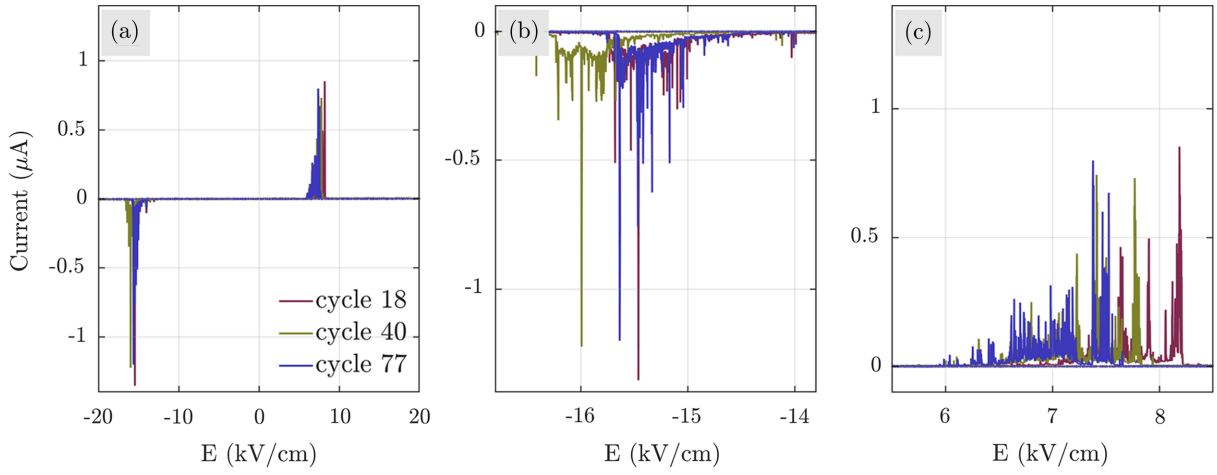


Figure 5
(*a*) Measured current as a function of electric field for three different electric-field cycles. Panels (*b*) and (*c*) show magnified views of regions switching from ↑ to ↓ and ↓ to ↑, respectively.

as well as in their height. Albeit certainly interesting, the further analysis of these distributions is beyond the scope of this work.

4. Strain-field dependence

Fig. 4(*d*) demonstrates a typical 'butterfly'-shaped dependence of the Bragg peak position on the electric field. This behavior is common for strain-field dependences in ferroelectrics and is often considered as one of the fingerprints of ferroelectricity. For the calculation of the strain tensor elements $x_{ij}(E)$ we used the radial (along **h**) components of the relative Bragg peak shifts $(\Delta q_{\rm obs}/\langle q\rangle)(\mathbf{h}, E)$ and the following equation for the corresponding simulated values:

$$\frac{\Delta q_{\rm sim}}{\langle q\rangle}(\mathbf{h}, E) = -\frac{x_{ij}(E) h_{Ci} h_{Cj}}{|\mathbf{h}|^2}, \qquad (11)$$

where h_{Ci} are the components of the reciprocal lattice vector **h** in the Cartesian crystal physical coordinate system (Nye, 1985). The axes of this coordinate system are aligned with the crystallographic axes of the conventional unit cell. The Einstein summation rule was implemented over the repeated indices *ij* as is customary in crystal physics (Nye, 1985).

The space symmetry group $Cmc2_1$ (the crystal class *mm2*) restricts the number of non-zero strain coefficients to three (x_{11}, x_{22}, x_{33}). Their numerical values are obtained by minimizing the sum of $(\Delta q_{\rm obs}/\langle q\rangle - \Delta q_{\rm sim}/\langle q\rangle)^2$ over all the measured **h** and at each point of the electric-field cycle. Fig. 6 shows observed and simulated relative shifts for five selected reflections, while similar data for all 42 measured reflections are provided in Supplementary Information 2.

Fig. 7 shows three resulting strain components. The straight sections of the strain-field curves can be used to estimate the piezoelectric coefficients from

$$d_{kij} = \frac{\partial x_{ij}}{\partial E_k}. \qquad (12)$$

The corresponding linear fits for ↑ and ↓ domain states as well as the determined piezoelectric coefficients d_{311}, d_{322} and

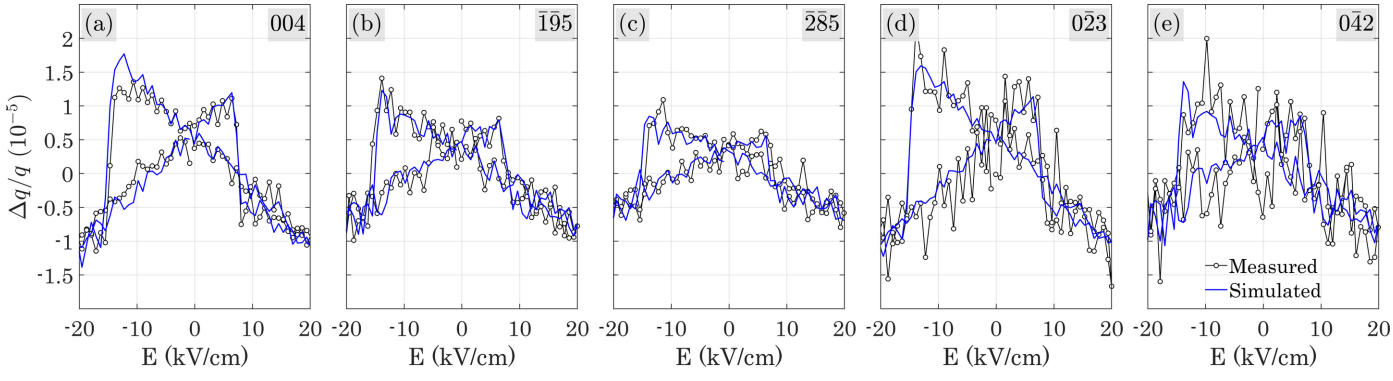


Figure 6
Comparison between the observed and simulated relative Bragg peak shifts $\Delta q/\langle q\rangle$ as a function of electric field for five representative reflections. The observed data (open circles) exhibit the characteristic butterfly-shaped response associated with ferroelectric strain behavior, while the simulated curves (blue lines) are obtained by refining the non-zero strain-tensor components using equation (11), closely reproducing the observed trends. Results for all 42 analyzed reflections are provided in Supplementary Information 2.

Table 5
The extracted piezoelectric coefficients.

For comparison, those estimated by Recker *et al.* (1974) are given.

	This work (domain ↓ and ↑)		Recker *et al.*
d_{311} (pC N^{-1})	−5.2 ± 0.5	7.4 ± 1.2	−4.2 ± 0.4
d_{322} (pC N^{-1})	1.1 ± 0.8	−1.8 ± 1.3	2.5 ± 0.3
d_{333} (pC N^{-1})	8.5 ± 0.2	−8.7 ± 0.2	8.1 ± 0.2

d_{333} are shown in Fig. 7. In addition, the piezoelectric coefficients listed in Table 5 closely match the literature values reported by Recker *et al.* (1974), thereby validating the reliability of the experimental results.

5. Structure refinements

5.1. The formalism

According to the kinematical theory of X-ray diffraction (Warren, 1990) the integrated intensity of a Bragg reflection **h** is proportional to the squared modulus of the structure factor:

$$I^{\delta}(\mathbf{h}) \propto \left|F^{\delta}(\mathbf{h})\right|^2, \tag{13}$$

where the structure factor corresponding to the domain δ is given by

$$F^{\delta}(\mathbf{h}) = \sum_{\mu=1}^{N_c} f_{\mu}(|\mathbf{h}|,\lambda)\exp\left(-\beta^{\delta}_{\mu,ij}h_ih_j\right)\exp\left(2\pi i\mathbf{h}\cdot\mathbf{r}^{\delta}_{\mu}\right). \tag{14}$$

Here $f_{\mu}(|\mathbf{h}|,\lambda) = f_{\mu}(|\mathbf{h}|) + f'_{\mu}(\lambda) + if''_{\mu}(\lambda)$ denotes the atomic scattering factor including wavelength-dependent resonant scattering corrections of the atom μ. $\beta^{\delta}_{\mu,ij}$ are the components of the tensors of the anisotropic atomic displacement parameters (ADPs) of the atom μ in the domain δ. The local symmetry of all Wyckoff positions in the child phase imposes $\beta^{\delta}_{\mu,12} = \beta^{\delta}_{\mu,13} = 0$ and keeps four ADPs per symmetry-independent atom ($ij = 11, 22, 33, 23$). Note that, while the sum in equation (14) runs over all the atoms in the conventional unit cell, the practical calculations of structure factor require $\mathbf{r}^{\delta}_{\mu}$ and $\beta^{\delta}_{\mu,ij}$ values for symmetry-independent atoms and the symmetry operations of the corresponding space symmetry group.

Table 6
The numerical values of resonant scattering corrections $f'_{\mu}(\lambda)$ and $f''_{\mu}(\lambda)$ for Ba, Mg and F atoms at the wavelength λ = 1.5405 Å.

	Ba	Mg	F
f'	−0.971	0.176	0.075
f''	8.504	0.181	0.055

As described in Section 2.2, atomic positions $\mathbf{r}^{\delta}_{\mu}$ can be parametrized in terms of SM amplitudes A^{δ}_{m} [equation (4)]. Furthermore, according to (5), the switching from the reference domain ↑ to the domain ↓ is achieved by $A^{\downarrow}_{m} = -A^{\uparrow}_{m}$ for all the Γ^{-}_{2} and $A^{\downarrow}_{m} = A^{\uparrow}_{m}$ for all the Γ^{+}_{1} SM amplitudes respectively. The transformation of anisotropic ADPs between domains is outlined in Appendix *B*. Accordingly, we introduce the structure factors for two domains in the form

$$F^{\uparrow}(\mathbf{h}) = F\left(\mathbf{h};\{A^{\uparrow}_{m}\},\{\beta^{\uparrow}_{\mu,ij}\}\right), \quad F^{\downarrow}(\mathbf{h}) = F\left(\mathbf{h};\{A^{\downarrow}_{m}\},\{\beta^{\downarrow}_{\mu,ij}\}\right) \tag{15}$$

and define the corresponding calculated intensity contrast as

$$C_{\rm calc}(\mathbf{h}) = \frac{\left|F^{\uparrow}(\mathbf{h})\right|^2 - \left|F^{\downarrow}(\mathbf{h})\right|^2}{I^{\uparrow\downarrow}(\mathbf{h})}. \tag{16}$$

$I^{\uparrow\downarrow}(\mathbf{h})$ corresponds to the state in which both domains are present in equal proportions:

$$I^{\uparrow\downarrow}(\mathbf{h}) = \tfrac{1}{2}\left(\left|F^{\uparrow}(\mathbf{h})\right|^2 + \left|F^{\downarrow}(\mathbf{h})\right|^2\right). \tag{17}$$

The role of the resonant scattering correction $if''_{\mu}(\lambda)$ is critical because it underpins the non-zero values of (16). Given their importance, for the reader's convenience we present in Table 6 the numerical values (Kissel *et al.*, 1995) of the resonant scattering corrections for Ba, Mg and F atoms at the Cu $K\alpha_1$ wavelength.

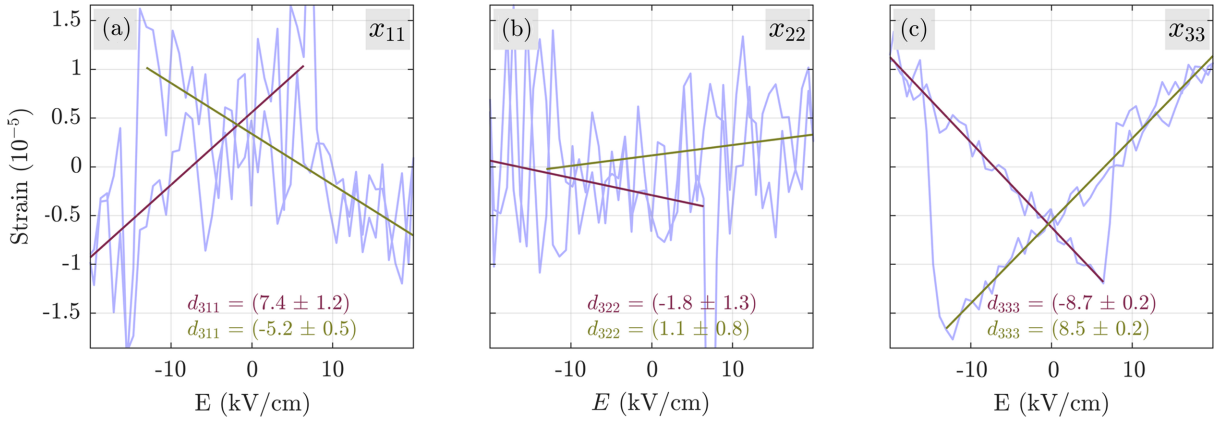


Figure 7
The electric-field dependence of the strain components x_{11}, x_{22}, x_{33}, obtained as a result of the refinement using Bragg peak shifts of 42 reflections and equation (11) for the strain components. Piezoelectric coefficients d_{311}, d_{322} and d_{333} were determined by regression in the linear regimes. The numerical values of the piezoelectric coefficients are given in units of pC N^{-1}.

5.2. The refinements

We performed the structure refinement through minimization of the error sum χ^2 over $N_{obs} = 42$ measured $C_{obs}(\mathbf{h})$ and their uncertainties $\sigma(\mathbf{h})$:

$$\chi^2 = \sum_{\mathbf{h}} \sigma^{-2}(\mathbf{h})\left[C_{obs}(\mathbf{h}) - C_{calc}(\mathbf{h})\right]^2. \quad (18)$$

The minimization of χ^2 was carried out using custom MATLAB scripts and the MATLAB *Optimization Toolbox* (The MathWorks Inc., Natick, MA, USA). In addition to determining the refined parameter values, the refinement procedure was used to calculate the corresponding standard uncertainties and parameter-correlation coefficients ρ_{mn} from the covariance matrix of the least-squares refinement [see *e.g.* Taylor (1982)].

In addition to the actively minimized χ^2 value, the refinement results were quantified using the weighted R factor

$$R_\omega = \frac{\sum_{\mathbf{h}} \sigma^{-1}(\mathbf{h})\left|C_{obs}(\mathbf{h}) - C_{calc}(\mathbf{h})\right|}{\sum_{\mathbf{h}} \sigma^{-1}(\mathbf{h})\left|C_{obs}(\mathbf{h})\right|} \quad (19)$$

and the goodness of fit

$$\mathrm{GoF} = \left(\frac{\chi^2}{N_{obs} - N_{par}}\right)^{1/2} \quad (20)$$

and validated by the Mg—F BVS according to (9) and MgF_6 octahedron distortion parameters D and L according to (6). Prior to refinement, both χ^2 and R_ω were evaluated for the S1/S2 structures to assess how well these models reproduce the observed intensity contrasts.

Each refined structure was shifted along the [001] direction to satisfy the condition of the closest proximity to S0 as described by equations (7) and (8). As explained in Section 2, this procedure removes the ambiguity associated with the arbitrary origin choice along the $\mathbf{a}_3$ axis and effectively reduces the number of independent refinable parameters by one. In practice, the Γ_2^- mode responsible for the displacement of the Ba atom along [001] was held fixed during the refinement, while the corresponding origin shift was applied afterwards.

Five refinement approaches (RA1–RA5) were implemented, differing in the treatment of ADPs while refining all 11 independent SMs.

Table 7
The results of the refinement achieved using refinement approaches RA1–RA4.

N_{par} corresponds to the number of refinable parameters. χ^2, R_ω and GoF are defined in equations (18), (19) and (20). max$|\rho|$ denotes the largest absolute value of the parameter-correlation coefficient; the complete correlation matrices are provided in Supplementary Information 4. The columns S1 and S2 correspond to the previously reported structural models refined with all structural parameters fixed.

	S1	RA1	S2	RA2	RA3	RA4
N_{par}	0	11	0	11	16	19
χ^2	60	48	110	56	52	13
R_ω (%)	4.4	4.0	6.0	3.9	3.9	1.9
GoF	–	1.24	–	1.34	1.41	0.75
max$\|\rho\|$	–	0.73	–	0.66	0.64	0.90
BVS	1.93	1.96	1.96	1.96	2.04	1.95
D (10^{-3})	0.71	0.95	0.82	0.74	1.22	0.72
L (10^{-3})	1.28	1.28	1.30	1.35	1.84	1.49

(i) RA1 and RA2 were conducted with the anisotropic ADPs fixed at the literature S1 and S2 values, respectively. This yielded 11 refinable parameters corresponding to the SM amplitudes A_m of the reference domain alone.

(ii) RA3 was performed using one refinable isotropic ADP per symmetry-independent atom, resulting in 11 SM amplitudes + 6 isotropic ADPs. To avoid the correlation between the ADP parameters, one ADP value was fixed, resulting in 16 free parameters. The initial isotropic ADPs were obtained by reduction of the anisotropic ADPs $\beta^{\delta}_{\mu,ij}$ of the S1 structure to their best isotropic representation.

(iii) RA4 extended RA3 by refining full anisotropic ADPs for Ba atoms, resulting in 11 SM amplitudes + 4 anisotropic ADPs (Ba) + 5 isotropic ADPs (Mg, F). With one ADP value fixed, this model contained 19 free parameters.

(iv) RA5 employed the full anisotropic model, including 11 SM amplitudes + 24 anisotropic ADPs (4 per symmetry-independent atom). With one fixed ADP, the model is described by 34 refined parameters. Because of the low data-to-parameter ratio (42 to 34), this refinement should be regarded as over-parameterized and the resulting parameter values interpreted with caution. Nevertheless, we performed this refinement to estimate the maximum achievable improvement in the agreement between the observed and calculated intensity contrasts.

Table 7 lists the number of refined parameters for each approach along with χ^2, R_ω, the maximum absolute value of

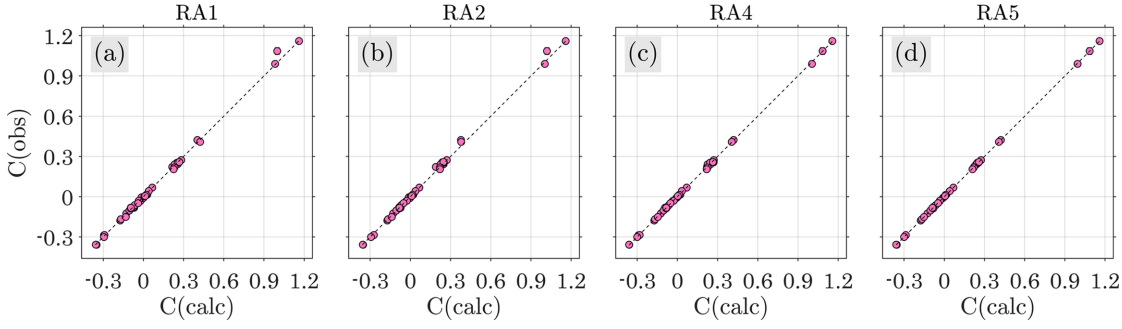


Figure 8
Parsons plots demonstrating the quality of fit for different refinement approaches.

Table 8
The SM amplitude values (organized similarly to Table 3) obtained using different refinement approaches.

The S1S2 amplitude shows the SM amplitudes averaged from the literature S1/S2 structures. The SM amplitudes are given in the units of Å. The amplitude of mode 1 (the Ba1 displacement mode) is not an independently refined parameter in RA1–RA4; its reported value results from the origin-shift procedure described by equations (7) and (8) and is therefore given without a standard uncertainty.

MN	Name (*Cmcm*[0,0,0])	Ferroelectric	$A^{(S1S2)}$	$A^{(RA1)}$	$A^{(RA2)}$	$A^{(RA3)}$	$A^{(RA4)}$
1	GM2-(a)[Ba1:c:dsp]B1(a)	F	0.239 (7)	0.2450	0.2466	0.2484	0.2409
3	GM2-(a)[Mg1:c:dsp]B1(a)	F	−0.0464 (3)	−0.026 (6)	−0.052 (6)	−0.046 (8)	−0.054 (4)
6	GM2-(a)[F1:a:dsp]Bu_2(a)	F	−0.548 (3)	−0.546 (6)	−0.542 (6)	−0.545 (7)	−0.540 (4)
8	GM2-(a)[F2:f:dsp]A′_2(a)	F	0.335 (8)	0.333 (5)	0.337 (5)	0.340 (6)	0.329 (3)
11	GM2-(a)[F3:c:dsp]B1(a)	F	−0.118 (7)	−0.14 (1)	−0.13 (1)	−0.14 (2)	−0.113 (9)
5	GM2-(a)[F1:a:dsp]Bu_1(a)	N	−0.501 (3)	−0.51 (2)	−0.52 (2)	−0.545 (7)	−0.52 (1)
7	GM2-(a)[F2:f:dsp]A′_1(a)	N	−0.434 (9)	−0.46 (2)	−0.45 (2)	−0.41 (2)	−0.42 (1)
2	GM1+(a)[Ba1:c:dsp]A1(a)	N	0.8367 (1)	0.834 (4)	0.829 (4)	0.863 (3)	0.843 (4)
4	GM1+(a)[Mg1:c:dsp]A1(a)	N	0.352 (6)	0.356 (9)	0.351 (9)	0.35 (1)	0.342 (6)
9	GM1+(a)[F2:f:dsp]A′_1(a)	N	−0.76 (3)	−0.79 (2)	−0.80 (2)	−0.89 (3)	−0.77 (2)
10	GM1+(a)[F2:f:dsp]A′_2(a)	N	−0.16 (2)	−0.153 (8)	−0.151 (8)	−0.169 (9)	−0.157 (5)
12	GM1+(a)[F3:c:dsp]A1(a)	N	0.449 (7)	0.43 (2)	0.42 (2)	0.42 (2)	0.48 (1)

the correlation coefficient max$|\rho|$, BVS, and MgF_6 octahedral distortion parameters D and L. In addition, the progress of the fit quality with increasing complexity of the model can be further inspected using the Parsons plots (Parsons *et al.*, 2013) in Fig. 8. These simple plots draw $C_{obs}(\mathbf{h})$ versus $C_{calc}(\mathbf{h})$ and thus serve as a helpful visual aid to assess the resulting quality of fit. Supplementary Information 3 shows the full list of observed and simulated intensity contrasts for the RA4 approach.

The optimization of the SM amplitudes alone (RA1/RA2) resulted in a moderate reduction of χ^2 from 60 to 48 for S1 and from 110 to 56 for S2. Using isotropic but refinable ADPs (RA3) resulted in a similar $\chi^2 = 52$. The transition from RA3 to RA4 produces the largest improvement in the goodness of fit, reducing χ^2 to 13 and GoF to 0.75, while introducing only three additional refinable parameters. This observation indicates that the measured switching contrasts contain substantial information about the anisotropic displacement tensor of Ba atoms. This fact is consistent with the dominant contribution of Ba to both the normal and resonant scattering amplitudes. The decrease of the GoF below unity, together with the maximum parameter-correlation coefficient reaching 0.90, indicates that this refinement strategy is approaching the limit of what can be reliably refined from the available data. The subsequent RA5 refinement yields a further reduction of χ^2 to 2.6 and GoF to 0.57, but at the cost of a substantially increased number of refinable parameters and very strong correlations between them. Together with a GoF substantially below unity, this indicates that RA5 is over-parameterized with respect to the available data. The restricted number of measured reflections necessarily limits the complexity of the structural model that can be reliably refined, particularly with respect to anisotropic ADPs. We therefore regard RA5 primarily as an estimate of the upper limit of achievable fit quality, whereas RA4 represents the most physically meaningful refinement model.

Table 8 provides the resulting SM amplitudes for the average of S1/S2 structures and for the refined RA1, RA2, RA3 and RA4 structures. It shows that the disagreement between the literature S1/S2 structures and the refined structures is well within the uncertainty ranges. As mentioned earlier, RA5 can be regarded as over-parameterized due to the limited data-to-parameter ratio. Therefore, on the basis of the achieved goodness of fit, we continue the discussion below with the RA4 results, which combine low χ^2 with a moderate number of parameters. The lists of ADPs together with the list of correlation coefficients between the parameters are provided in Supplementary Information 4.

6. Discussion

The structure refinements presented above provide crystallographic information on the end states corresponding to the ↑ and ↓ domains. Fig. 9 illustrates these states, while Supplementary Information 5 presents full animations of possible structural paths connecting the structures of both domains. These materials show that the switching between the two ferroelectric domains is driven by rotation of non-rigid MgF_6 octahedra, accompanied by Ba-atom displacements. The figure also highlights the role of the anisotropic ADPs of Ba atoms and flipping of the corresponding displacement ellipsoids upon switching between ferroelectric domains.

The pronounced sensitivity to these anisotropic ADPs of Ba should not be viewed as evidence that Ba is the dominant microscopic contributor to the ferroelectric distortion. Rather, Ba acts as the strongest scatterer channel in the present resonant scattering experiment. The refined SM amplitudes nevertheless demonstrate that several of the largest ferroelectric distortions are associated with fluorine displacements, which are refined with reasonable uncertainty (Table 8).

The discussion below addresses the possible structural and microstructural pathways of the domain switching. A key experimental limitation must be first acknowledged. The X-ray diffraction data used for structure refinement, illustrated *e.g.* for a representative reflection in Fig. 4 and for the full data set in Supplementary Information 1, are effectively averaged over 101 electric-field cycles. This averaging is unavoidable, as acquisition of a complete rocking curve requires physical rotation of the crystal, such that each ω angle sampled a distinct field cycle. Consequently, each rocking

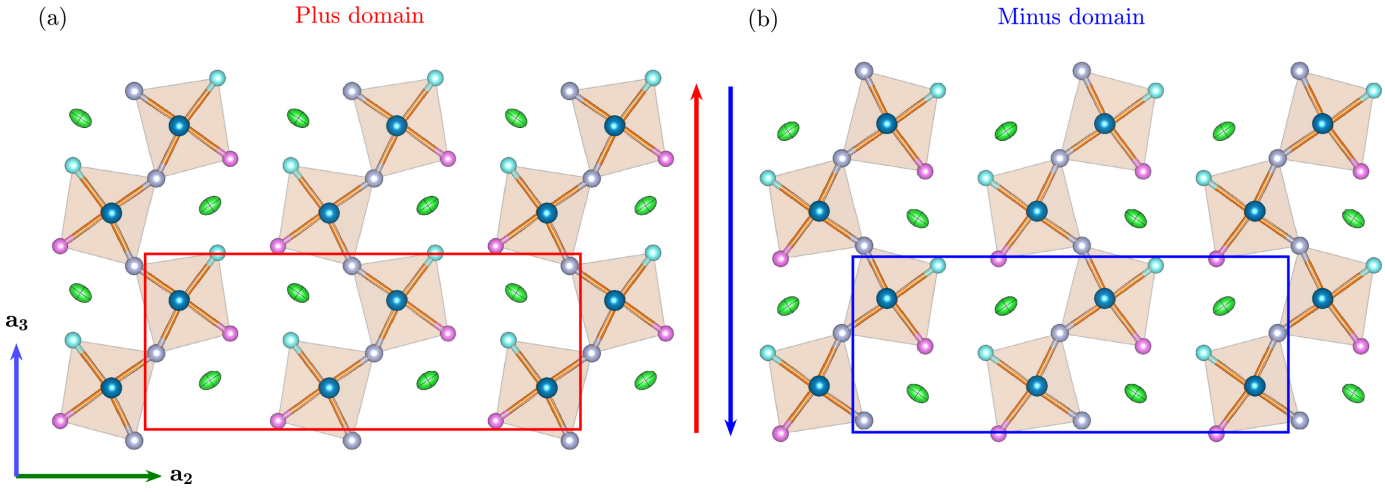


Figure 9
Schematic representation of the $BaMgF_4$ structures obtained from refinement approach RA4, viewed along the crystallographic $\mathbf{a}_1$ axis. Panels (*a*) and (*b*) correspond to the ↑ and ↓ ferroelectric domain variants, respectively. The conventional unit cells are outlined by red and blue rectangles. The animations provided in the Supplementary Information 5 illustrate a representative continuous switching pathway that transforms one domain structure into the other.

curve represents a cycle-averaged structural response rather than the instantaneous structure at a given moment during switching. The impact of this averaging is evident from comparison of the cycle-averaged switching current [Fig. 4(*b*)] with the single-cycle current in Fig. 5. Whereas the averaged current exhibits a smooth behavior, individual cycles are characterized by sharp, discrete Barkhausen-like current pulses, indicative of avalanche-type switching events (Tagantsev *et al.*, 2010). This observation suggests that polarization reversal might proceed through a sequence of localized, discontinuous processes rather than a homogeneous, 'coherent' transformation.

Despite this limitation, cycle-average data allow meaningful discussion of hypothetical switching mechanisms. To enable such a discussion, we simulated the evolution of diffraction intensities along three hypothetical pathways from ↑ to ↓. A single scalar coordinate η was introduced, varying continuously between the pure domain state values $\eta = +1$ and $\eta = -1$ along the pathway. Both displacive SM amplitudes and ADP tensors entering the structure factor were modified as described in the next paragraph, so that $A'_m(\eta)$ and $\beta'_{\mu,ij}(\eta)$ were used instead of static A_m and $\beta_{\mu,ij}$.

Two 'structural' switching paths were considered, PW1 and PW2. For PW1, the Γ_2^- SM amplitudes were scaled as $A'_m(\eta) = \eta A_m$ so that these SM amplitudes change sign between domains. Because, according to equation (5), Γ_1^+ SM amplitudes do not change sign upon polarization reversal, they were scaled as $A'_m(\eta) = \eta^2 A_m$. This choice avoids the non-analytical behavior of $|\eta|$ at $\eta = 0$ and is consistent with the interpretation of Γ_1^+ SMs as secondary distortions coupled quadratically to the primary ones. For PW2, only Γ_2^- SM amplitudes were scaled as in PW1, while the Γ_1^+ SM amplitudes were fixed, resulting in the shortest straight-line trajectory connecting the pure domain states. The ADP components

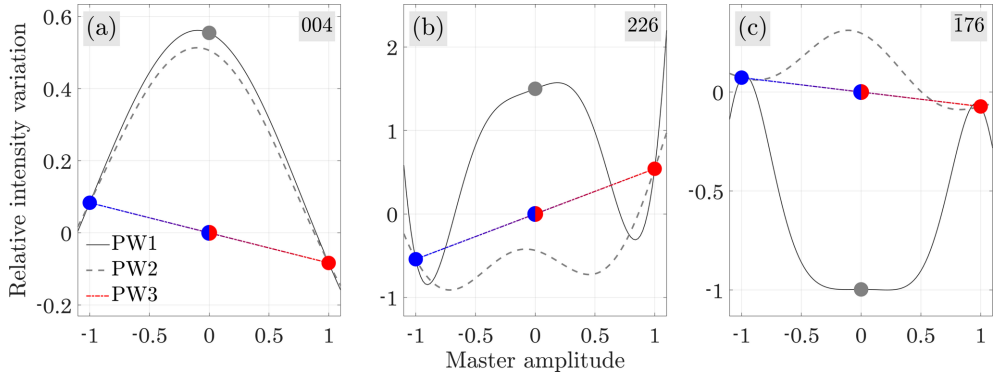


Figure 10
Simulated dependence of the relative diffraction intensity according to equations (21) and (22) on the switching coordinate η for three representative Bragg reflections. The curves correspond to three hypothetical switching pathways: PW1 and PW2 represent uniform 'structural' switching trajectories, while PW3 describes domain-wall-mediated switching. Blue and red circles indicate the fully switched ↓ and ↑ domain states; the gray circle represents the S0 state; the two-colored symbol at $\eta = 0$ marks the equal-domain mixed state.

$\beta'_{\mu,ij}(\eta)$ were defined using simple interpolation between $\beta^{\uparrow}_{\mu,ij}$ and $\beta^{\downarrow}_{\mu,ij}$ values. Accordingly, the diffraction intensity of PW1/PW2 switching pathways was simulated as

$$I^{(1,2)}_{\rm calc}(\mathbf{h},\eta) = \frac{\left|F\left(\mathbf{h};\left\{A'_m(\eta)\right\},\left\{\beta'_{\mu,ij}(\eta)\right\}\right)\right|^2 - I^{\uparrow\downarrow}(\mathbf{h})}{I^{\uparrow\downarrow}(\mathbf{h})}. \quad (21)$$

Here, we also neglect the effect of the small field-induced changes in reciprocal-lattice vector lengths on the calculated structure factors [see *e.g.* Gorfman *et al.* (2005)].

In contrast, PW3 represents a non-uniform switching mechanism dominated by domain-wall motion, for which the diffraction intensity is described as an incoherent sum of contributions from coexisting domains:

$$\begin{aligned} I^{(3)}_{\rm calc}(\mathbf{h},\eta) &= \frac{1}{I^{\uparrow\downarrow}(\mathbf{h})}\left[\frac{1+\eta}{2}\left|F^{\uparrow}(\mathbf{h})\right|^2 + \frac{1-\eta}{2}\left|F^{\downarrow}(\mathbf{h})\right|^2 - I^{\uparrow\downarrow}(\mathbf{h})\right] \\ &= \frac{\eta}{2}C_{\rm calc}(\mathbf{h}). \end{aligned} \quad (22)$$

The simulated intensity evolutions for representative Bragg reflections are shown in Fig. 10. Remarkably, PW1 and PW2 are associated with pronounced transient intensity variations, substantially exceeding the intensity difference between the end states. For example, for the 004 reflection the observed switching contrast is approximately −15%, whereas PW1 predicts a transient intensity increase of nearly 50%. Even larger transient effects are predicted for other reflections, such as 226 and $\bar{1}76$.

Importantly, no such transient intensity variations are observed. Although the actual switching events are represented by only two to three data points per cycle (Fig. 4), the magnitude of the predicted transient effects for PW1 and PW2 is sufficiently large that at least partial signatures would be expected if coherent switching occurred on the experimental timescale. Their absence therefore supports a non-uniform switching mechanism, consistent with PW3 and dominated by the nucleation and motion of domain walls.

An alternative possibility of coherent uniform switching occurring on timescales much shorter than the temporal resolution of the present experiment cannot be completely excluded. However, resolving such ultrafast processes would require diffraction measurements capable of recording integrated intensities without sample rotation. This could be achieved, for example, using broadband ('pink') X-ray radiation or bent-crystal monochromators, provided that the reciprocal-lattice peak remains fully covered within the thickness of the Ewald sphere resulting from the available wavelength bandwidth. For the present peak widths (∼0.5°), a relative bandwidth of approximately 3% would be required. Such experiments remain challenging both technically and because of potential beam damage. In addition, the possibility that the switching mechanism will be affected by the synchrotron beam cannot be excluded.

7. Conclusions

We have introduced and demonstrated a new structure-refinement strategy for uniaxial ferroelectric crystals that is based on electric-field-induced Bragg intensity contrasts rather than on absolute diffraction intensities. We exploit reversible switching between two ferroelectric domains and measure the corresponding Bragg intensities at identical diffraction geometries. The approach effectively eliminates the influence of absorption and similar systematic effects that limit conventional single-crystal refinement. The method is therefore well suited for *in situ* diffraction study of ferroelectrics under applied electric fields and for materials where reliable absorption corrections are difficult or impossible to achieve.

Applied to $BaMgF_4$, the approach enabled refinement of displacive symmetry-mode amplitudes describing the deviation from a hypothetical parent paraelectric phase. The refined mode amplitudes are in good agreement with previously reported structural models, and the agreement factors achieved are substantially improved once anisotropic atomic displacement parameters (particularly for Ba) are considered. This highlights the importance of an adequate thermal-motion model when interpreting X-ray diffraction contrasts in heavy-atom ferroelectrics.

Beyond static structural refinement, the method provides insight into polarization-switching mechanisms. Comparison between observed and simulated intensity evolutions suggests a non-uniform switching process dominated by nucleation and domain-wall motion, in agreement with the Barkhausen-like current pulses detected during individual switching cycles. While ultrafast coherent processes below the present temporal resolution cannot be entirely excluded, the results put strong constraints on switching scenarios in $BaMgF_4$ under quasi-static electric fields.

More generally, the methodology presented here is applicable to uniaxial ferroelectrics and other polar materials where sufficiently large resonant scattering is present. It offers a robust route to isolating the structural degrees of freedom directly responsible for polarization, independent of many traditional crystallographic corrections, and naturally complements symmetry-mode tools such as *ISODISTORT*. The approach therefore opens new possibilities for quantitative X-ray crystallography of functional ferroic materials.

APPENDIX *A*

Choice of the unit cell origin in the BMF child phase

Like any ferroelectric, the BMF child phase possesses a structure with a floating unit cell origin. In particular, the space group type $Cmc2_1$ permits a continuous shift of the origin along the 2_1 axis parallel to [001]. This freedom complicates the comparison of crystal structures reported by different X-ray crystallographers, since differences arising purely from a unit cell origin shift are not always easy to identify visually. A common practical solution is to fix the coordinate of a selected atom, for example the z coordinate of an oxygen atom in rhombohedral perovskites (Megaw & Darlington, 1975).

Here we implement a more universal approach, which shifts the child structure to its point of closest proximity to the

Table 9
SM amplitudes B_m corresponding to a rigid translation of the entire structure by the lattice vector [001].

The first two columns list the mode number and the mode label (following the definitions in the main text). The third column indicates whether the mode contributes to the above rigid displacement ('F', ferroelectric) or not ('N', non-ferroelectric). All the Γ_1^+ are non-ferroelectric and therefore omitted from the table. The last column shows the numerical values of the SM amplitudes B_m for ferroelectric modes. The analysis shows that, in addition to non-ferroelectric Γ_1^+ modes, two Γ_2^- modes also do not contribute to the rigid [001] displacement.

MN	Mode label (*Cmcm*[0,0,0]...)	Ferroelectric	B_m (Å)
1	GM2-(a)[Ba1:c:dsp]B1(a)	F	8.23
3	GM2-(a)[Mg1:c:dsp]B1(a)	F	8.23
6	GM2-(a)[F1:a:dsp]Bu_2(a)	F	8.23
8	GM2-(a)[F2:f:dsp]A′_2(a)	F	11.64
11	GM2-(a)[F3:c:dsp]B1(a)	F	8.23
5	GM2-(a)[F1:a:dsp]Bu_1(a)	N	0
7	GM2-(a)[F2:f:dsp]A′_1(a)	N	0

parent structure. This procedure is suitable for describing structural distortions relative to the parent phase and for the application of the symmetry-mode formalism.

Given the mode-definition vectors $\mathbf{D}_{\mu m}$, we construct the matrix $\mathbf{M}$, which relates the column vector of atomic displacements $\mathbf{S_A}$ to the column vector of SM amplitudes $\mathbf{A}$:

$$\mathbf{S_A} = \mathbf{MA}. \tag{23}$$

The dimensions of $\mathbf{S_A}$, $\mathbf{M}$ and $\mathbf{A}$ are $3N_c \times 1$, $3N_c \times N_M$ and $N_M \times 1$, respectively.

Next, we construct a displacement vector $\mathbf{S_B}$ of size $3N_c \times 1$, which describes a rigid translation of the entire structure by [001]. This vector consists of N_c copies of the 3×1 column vector $(0, 0, 1)^T$ stacked consecutively. We then find the corresponding SM amplitude vector $\mathbf{B}$ which ensures that $\mathbf{S_B} = \mathbf{MB}$. The corresponding $\mathbf{B}$ can be calculated by least squares, minimizing $||\mathbf{S_B} - \mathbf{MB}||^2$. Since the distortion vector $\mathbf{S_B}$ belongs to the column space of $\mathbf{M}$, the minimum residual is zero, giving

$$\mathbf{B} = \left(\mathbf{M}^T\mathbf{M}\right)^{-1}\mathbf{M}^T\mathbf{S_B}. \tag{24}$$

Table 9 shows the resulting components of $\mathbf{B}$, which together generate a uniform displacement of the structure along [001]. The analysis also reveals whether a given symmetry mode is compatible with ferroelectricity. Modes that do not contribute to [001] rigid displacement are therefore marked as 'N' (non-ferroelectric) rather than 'F' (ferroelectric). Besides the clearly non-ferroelectric Γ_1^+ modes, two Γ_2^- modes do not contribute to the ferroelectric [001] displacement.

Finally, the SM amplitude vector $\mathbf{A}$ of the refined structure is adjusted by adding a uniform [001] origin shift according to $\mathbf{A} + t\mathbf{B}$. The scalar coefficient t is defined through equations (7) and (8). Equation (7) represents the sum of squared atomic displacements per primitive unit cell, ensuring a geometrically meaningful definition of the optimal origin choice.

Table 10
Transformation rules for the anisotropic ADPs of symmetry independent atoms when switching from the reference domain (↑) to the reversed domain ↓.

The first two columns identify the symmetry-independent atoms from Table 4. The third column introduces the independent anisotropic ADPs for the reference domain, while the last column gives the corresponding ADPs for the same atoms in the domain ↓. Depending on the atom, the domain reversal may leave the ADPs unchanged, reverse the sign of the β_{23} component or interchange the ADPs between atomic sites ($F2_1$ and $F2_2$).

AN	Atom label	Domain ↑	Domain ↓
1	Ba1	$\beta_{1,11}, \beta_{1,22}, \beta_{1,33}, \beta_{1,23}$	$\beta_{1,11}, \beta_{1,22}, \beta_{1,33}, -\beta_{1,23}$
2	Mg1	$\beta_{2,11}, \beta_{2,22}, \beta_{2,33}, \beta_{2,23}$	$\beta_{2,11}, \beta_{2,22}, \beta_{2,33}, -\beta_{2,23}$
3	F1	$\beta_{3,11}, \beta_{3,22}, \beta_{3,33}, \beta_{3,23}$	$\beta_{3,11}, \beta_{3,22}, \beta_{3,33}, \beta_{3,23}$
4	$F2_1$	$\beta_{4,11}, \beta_{4,22}, \beta_{4,33}, \beta_{4,23}$	$\beta_{5,11}, \beta_{5,22}, \beta_{5,33}, \beta_{5,23}$
5	$F2_2$	$\beta_{5,11}, \beta_{5,22}, \beta_{5,33}, \beta_{5,23}$	$\beta_{4,11}, \beta_{4,22}, \beta_{4,33}, \beta_{4,23}$
6	F3	$\beta_{6,11}, \beta_{6,22}, \beta_{6,33}, \beta_{6,23}$	$\beta_{6,11}, \beta_{6,22}, \beta_{6,33}, -\beta_{6,23}$

APPENDIX *B*

Changing the anisotropic ADPs of symmetry-independent atoms when switching between the domains (short description)

Calculation of the structure factors requires knowledge of the positions $\mathbf{r}_\mu$ and ADPs $\boldsymbol{\beta}_\mu$ of all the atoms in the unit cell. Although equation (14) involves a summation of all the atoms in the conventional unit cell, in practice it is sufficient to specify positions and ADPs for the symmetry-independent atoms. The positions and ADPs of all symmetry-equivalent atoms are generated using the symmetry operations of the space group and the standard transformation rules (Shmueli, 2008). For a symmetry operation $(\mathbf{R}|\mathbf{v})$, defined by the 3×3 rotation matrix $\mathbf{R}$ and a 3×1 translation vector $\mathbf{v}$, the atomic coordinates transform as

$$\mathbf{r}_\mu(\mathbf{R}|\mathbf{v}) = \mathbf{R}\mathbf{r}_\mu + \mathbf{v}, \tag{25}$$

while the corresponding anisotropic ADP tensor transforms according to

$$\boldsymbol{\beta}_\mu(\mathbf{R}|\mathbf{v}) = \mathbf{R}\boldsymbol{\beta}_\mu\mathbf{R}^T. \tag{26}$$

These relations are valid for generating symmetry-related atoms within a single domain, where $(\mathbf{R}|\mathbf{v})$ belongs to the space group of that domain. For all atoms in the BMF child phase equation (26) keeps all four ADPs unchanged or changes $\beta_{\mu,23}$ to $-\beta_{\mu,23}$.

ISODISTORT supports the SM parameterization of atomic displacements. This enables us to convert the position of an atom μ in the reference domain $\mathbf{r}_\mu^\uparrow$ to the position of the atom that is physically the same in the second domain $\mathbf{r}_\mu^\downarrow$. However, analogous parametrization and transformation of anisotropic ADPs are not yet supported. Therefore, the transformation of the ADPs associated with a given set of symmetry-independent atoms between domains must be derived separately. Formally, this transformation can be obtained as an extension of expression (26):

$$\boldsymbol{\beta}_\mu^\downarrow(\mathbf{R}|\mathbf{v}) = \left(\mathbf{R}_c\mathbf{R}_{\mu\nu}\right)\boldsymbol{\beta}_\nu^\uparrow\left(\mathbf{R}_c\mathbf{R}_{\mu\nu}\right)^T, \tag{27}$$

where $\mathbf{R}_c$ is the rotation matrix of the coset representative $(\mathbf{R}_c|\mathbf{v}_c)$ associated with the domain ↓, and $\mathbf{R}_{\mu\nu}$ is the rotation

matrix of the symmetry operator of the reference domain of the child space group $(\mathbf{R}_{\mu\nu}|\mathbf{v}_{\mu\nu})$ such that

$$\mathbf{r}_{\mu}^{\downarrow} = \left(\mathbf{R}_{\rm c}\mathbf{R}_{\mu\nu}\right)\mathbf{r}_{\nu}^{\uparrow} + \mathbf{R}_{\rm c}\mathbf{v}_{\mu\nu} + \mathbf{v}_{\rm c}. \tag{28}$$

The practical part of the procedure consists of identifying, for each symmetry-independent atom, the reference atom ν and the symmetry operator $(\mathbf{R}_{\mu\nu}|\mathbf{v}_{\mu\nu})$ such that the combined operation $(\mathbf{R}_{\rm c}\mathbf{R}_{\mu\nu}|\mathbf{R}_{\rm c}\mathbf{v}_{\mu\nu} + \mathbf{v}_{\rm c})$ maps $\mathbf{r}_{\nu}^{\uparrow}$ into $\mathbf{r}_{\mu}^{\downarrow}$.

For BMF, this analysis shows (Table 10) that domain reversal affects the ADPs differently for different atomic sites. For some atoms, the transformation results in a sign change of β_{23}. For other atoms, the ADP tensor remains invariant under domain reversal or is transferred between symmetry-independent fluorine sites.

Importantly, $C_{\rm calc}(\mathbf{h})$ remains unchanged if a constant β_0 is added to all the diagonal elements of the ADP tensors, *i.e.* $\beta_{\mu,11} \rightarrow \beta_{\mu,11} + \beta_0$, $\beta_{\mu,22} \rightarrow \beta_{\mu,22} + \beta_0$ and $\beta_{\mu,33} \rightarrow \beta_{\mu,33} + \beta_0$. Consequently, these parameters are not independently determined and exhibit a perfect correlation. To remove this redundancy and ensure a unique refinement, one of the diagonal ADP components must be fixed. In the present work, $\beta_{1,11}$ was fixed.

Acknowledgements

NL, SG and IB acknowledge Yuri Katz (Tel Aviv University) for his assistance with the experimental setup.

Funding information

The research of SG, NL and CR was supported by the German Research Foundation (DFG–Middle East program, grant No. 521034088). SG acknowledges support from the Israel Science Foundation (grant Nos. 1561/18, 1365/23) and the United States–Israel Binational Science Foundation (award No. 2018161). HT and GB acknowledge financial support from BMFTR through project No. 13N16923 'Kohärente Dauerstrichstrahlung im Vakuum-UV (UV-KrisP)'.

References

Aizu, K. (1966). *Phys. Rev.* **146**, 423–429.
Becker, P. J. & Coppens, P. (1974). *Acta Cryst.* A**30**, 129–147.
Bradley, C. J. & Cracknell, A. P. (2009). *The Mathematical Theory of Symmetry in Solids: Representation Theory for Point Groups and Space Groups*. Oxford University Press.
Brown, I. D. (2006). *The Chemical Bond in Inorganic Chemistry: The Bond Valence Model*. Oxford University Press.
Brown, I. D. & Altermatt, D. (1985). *Acta Cryst.* B**41**, 244–247.
Campbell, B. J., Stokes, H. T., Tanner, D. E. & Hatch, D. M. (2006). *J. Appl. Cryst.* **39**, 607–614.
Choe, H., Bieker, J., Zhang, N., Glazer, A. M., Thomas, P. A. & Gorfman, S. (2018). *IUCrJ* **5**, 417–427.
Damjanovic, D. (1998). *Rep. Prog. Phys.* **61**, 1267–1324.
DiDomenico, M. Jr, Eibschütz, M., Guggenheim, H. J. & Camlibel, I. (1969). *Solid State Commun.* **7**, 1119–1122.
Ederer, C. & Spaldin, N. A. (2006). *Phys. Rev. B* **74**, 024102.
Flack, H. D. (1983). *Acta Cryst.* A**39**, 876–881.
Flack, H. D. & Bernardinelli, G. (1999). *Acta Cryst.* A**55**, 908–915.
Flack, H. D. & Shmueli, U. (2007). *Acta Cryst.* A**63**, 257–265.
Garcia-Castro, A. C., Ibarra-Hernandez, W., Bousquet, E. & Romero, A. H. (2018). *Phys. Rev. Lett.* **121**, 117601.
Gingl, F. (1997). *Z. Anorg. Allg. Chem.* **623**, 705–709.
Gorfman, S., Choe, H., Zhang, G., Zhang, N., Yokota, H., Glazer, A. M., Xie, Y., Dyadkin, V., Chernyshov, D. & Ye, Z.-G. (2020). *J. Appl. Cryst.* **53**, 1039–1050.
Gorfman, S., Schmidt, O., Tsirelson, V., Ziolkowski, M. & Pietsch, U. (2013). *Z. Anorg. Allg. Chem.* **639**, 1953–1962.
Gorfman, S., Simons, H., Iamsasri, T., Prasertpalichat, S., Cann, D. P., Choe, H., Pietsch, U., Watier, Y. & Jones, J. L. (2016). *Sci. Rep.* **6**, 20829.
Gorfman, S., Spirito, D., Cohen, N., Siffalovic, P., Nadazdy, P. & Li, Y. (2021). *J. Appl. Cryst.* **54**, 914–923.
Gorfman, S., Tsirelson, V., Pucher, A., Morgenroth, W. & Pietsch, U. (2006). *Acta Cryst.* A**62**, 1–10.
Gorfman, S. V., Tsirelson, V. G. & Pietsch, U. (2005). *Acta Cryst.* A**61**, 387–396.
Haertling, G. H. (1999). *J. Am. Ceram. Soc.* **82**, 797–818.
Herr, S. J., Tanaka, H., Breunig, I., Bickermann, M. & Kühnemann, F. (2023). *Opt. Mater. Express* **13**, 2158–2164.
Kissel, L., Zhou, B., Roy, S. C., Sen Gupta, S. K. & Pratt, R. H. (1995). *Acta Cryst.* A**51**, 271–288.
Kowalczyk, R. M., Kemp, T. F., Walker, D., Pike, K. J., Thomas, P. A., Kreisel, J., Dupree, R., Newton, M. E., Hanna, J. V. & Smith, M. E. (2011). *J. Phys. Condens. Matter* **23**, 315402.
Kreisel, J., Noheda, B. & Dkhil, B. (2009). *Phase Transit.* **82**, 633–661.
Lines, M. E. & Glass, A. M. (1979). *Principles and Applications of Ferroelectrics and Related Materials*. Oxford University Press.
Megaw, H. D. & Darlington, C. N. W. (1975). *Acta Cryst.* A**31**, 161–173.
Meyer, M. (2015). *Acta Cryst.* A**71**, s496.
Momma, K. & Izumi, F. (2011). *J. Appl. Cryst.* **44**, 1272–1276.
Nye, J. F. (1985). *Physical Properties of Crystals: Their Representation by Tensors and Matrices*. Clarendon Press.
Ozawa, Y., Pressprich, M. R. & Coppens, P. (1998). *J. Appl. Cryst.* **31**, 128–135.
Park, S.-E. & Shrout, T. R. (1997). *J. Appl. Phys.* **82**, 1804–1811.
Parsons, S., Flack, H. D. & Wagner, T. (2013). *Acta Cryst.* B**69**, 249–259.
Posse, J. M., Friese, K. & Grzechnik, A. (2011). *J. Phys. Condens. Matter* **23**, 215401.
Posse, J. M., Grzechnik, A. & Friese, K. (2009). *Acta Cryst.* B**65**, 576–586.
Recker, K., Wallrafen, F. & Haussühl, S. (1974). *J. Cryst. Growth* **26**, 97–100.
Schmidt, O., Gorfman, S., Bohatý, L., Neumann, E., Engelen, B. & Pietsch, U. (2009). *Acta Cryst.* A**65**, 267–275.
Shmueli, U. (2008). Editor. *International Tables for Crystallography*, Vol. B, *Reciprocal Space*, 3rd ed. Springer Netherlands.
Stokes, H. T. & Hatch, D. M. (2005). *J. Appl. Cryst.* **38**, 237–238.
Tagantsev, A. K., Cross, L. E. & Fousek, J. (2010). *Domains in Ferroic Crystals and Thin Films*. Springer.
Taylor, J. R. (1982). *An Introduction to Error Analysis: The Study of Uncertainties in Physical Measurements*. Oxford University Press.
Trolier-McKinstry, S., Zhang, S., Bell, A. J. & Tan, X. (2018). *Annu. Rev. Mater. Res.* **48**, 191–217.
Uchino, K. (2017). Editor. *Advanced Piezoelectric Materials: Science and Technology*, 2nd ed. Woodhead Publishing.
Vasiljevic, M., Kollár, M., Spirito, D., Riemer, L., Forró, L., Horváth, E., Gorfman, S. & Damjanovic, D. (2022). *Adv. Funct. Mater.* **32**, 2204898.
Warren, B. E. (1990). *X-ray Diffraction*. Dover Publications.